JOPSS
JAEA Originated Papers Searching System

日本原子力研究開発機構機関リポジトリ
Japan Atomic Energy Agency Institutional Repository

Title	Laser-driven neutron generation realizing single-shot resonance spectroscopy
Author(s)	Yogo Akifumi, Lan Z., Arikawa Yasunobu, Abe Yuki, Mirfayzi S. R., Wei T., Mori Takato, Golovin D., Hayakawa Takehito, Iwata Natsumi, Fujioka Shinsuke, Nakai Mitsuo, Sentoku Yasuhiko, Mima Kunioki, Murakami Masakatsu, Koizumi Mitsuo, Ito Fumiaki, Lee J., Takahashi Tone, Hironaka Kota, Kar S., Nishimura Hiroaki, Kodama Ryosuke
Citation	Physical Review X, 13(1), p.011011_1 - 011011_12
Text Version	Published Journal Article
URL	https://jopss.jaea.go.jp/search/servlet/search?5072497
DOI	https://doi.org/10.1103/PhysRevX.13.011011
Right	Published by the American Physical Society under the terms of the Creative Commons Attribution 4.0 International license. Further distribution of this work must maintain attribution to the author(s) and the published article's title, journal citation, and DOI.

Japan Atomic Energy Agency

Laser-Driven Neutron Generation Realizing Single-Shot Resonance Spectroscopy

A. Yogo,[1,*] Z. Lan,[1] Y. Arikawa,[1] Y. Abe,[1] S. R. Mirfayzi,[2] T. Wei,[1] T. Mori,[1] D. Golovin,[1] T. Hayakawa,[3] N. Iwata,[1] S. Fujioka,[1] M. Nakai,[1] Y. Sentoku,[1] K. Mima,[1] M. Murakami,[1] M. Koizumi,[4] F. Ito,[4] J. Lee,[4] T. Takahashi,[4] K. Hironaka,[4] S. Kar,[5] H. Nishimura,[6] and R. Kodama[1]

[1]*Institute of Laser Engineering, Osaka University, Suita, Osaka 565-0871, Japan*
[2]*Tokamak Energy Ltd, 173 Brook Drive, Milton, Abingdon OX14 4SD, United Kingdom*
[3]*National Institutes for Quantum and Radiological Science, and Technology, Tokai, Ibaraki 319-1106, Japan*
[4]*Japan Atomic Energy Agency, Tokai, Ibaraki 319-1195, Japan*
[5]*Centre for Plasma Physics, School of Mathematics and Physics, Queen's University Belfast, Belfast BT7 1NN, United Kingdom*
[6]*Fukui University of Technology, Fukui, 910-0028, Japan*

(Received 11 October 2021; revised 15 November 2022; accepted 20 December 2022; published 31 January 2023)

Neutrons are powerful tools for investigating the structure and properties of materials used in science and technology. Recently, laser-driven neutron sources (LDNS) have attracted the attention of different communities, from science to industry, in a variety of applications, including radiography, spectroscopy, security, and medicine. However, the laser-driven ion acceleration mechanism for neutron generation and for establishing the scaling law on the neutron yield is essential to improve the feasibility of LDNS. In this paper, we report the mechanism that accelerates ions with spectra suitable for neutron generation. We show that the neutron yield increases with the fourth power of the laser intensity, resulting in the neutron generation of 3×10^{11} in 4π at a maximum, with 1.1×10^{19} W cm^{-2}, 900 J, 1.5 ps lasers. By installing a "hand-size" moderator, which is specially designed for the LDNS, it is demonstrated that the efficient generation of epithermal (0.1–100 eV) neutrons enables the single-shot analysis of composite materials by neutron resonance transmission analysis (NRTA). We achieve the energy resolution of 2.3% for 5.19-eV neutrons 1.8 m downstream of the LDNS. This leads to the analysis of elements and isotopes within sub-μs times and allows for high-speed nondestructive inspection.

DOI: 10.1103/PhysRevX.13.011011

Subject Areas: Interdisciplinary Physics, Nonlinear Dynamics, Plasma Physics

I. INTRODUCTION

Light has become an indispensable tool for science and industry to explore and control the structure and properties of matter. Some game-changing works [1–3] paved the way for a novel scheme enabling laser acceleration of ions up to mega-electron volt (MeV) energies from a region of micrometers. Recently, laser-driven neutron sources (LDNS) [4–15] have been attracting interest for a number of reasons, including (i) the compactness in the range of millimeters, (ii) the capability to generate short bursts of pulses with time durations shorter than ns at the source, (iii) multiple-beam generation such as x rays, electrons, and neutrons [16], and (iv) high transportability of laser light expanding the usable area of neutrons.

LDNS research using high-intensity lasers was pioneered by studies using D-D fusion [4–6] and was expanded by works utilizing secondary nuclear reactions of MeV-energy ions [7–15] or electrons [17] accelerated by lasers. Alejo *et al.* [13] enhanced the neutron yield with deuteron acceleration from a layer of solid heavy water. Kleinschmidt *et al.* [14] reported 1.4×10^{10} neutron generation per steradian (sr) via efficient ion acceleration with a laser of 10^{20} W cm^{-2}. Hence, elucidation of the laser-driven ion acceleration mechanism is essential to control and enhance neutron generation.

The LDNS predominantly generate fast neutrons in the energy range of MeV. However, the neutron reaction cross sections on atomic nuclei increase with decreasing neutron energy. For instance, nuclear resonance absorptions are induced in the energy region of 1–1000 eV depending on nuclear species, which provides a tool for nondestructive analysis of isotopes. The low-energy neutrons are required for broader applications. Recently,

*yogo-a@ile.osaka-u.ac.jp

Published by the American Physical Society under the terms of the Creative Commons Attribution 4.0 International license. Further distribution of this work must maintain attribution to the author(s) and the published article's title, journal citation, and DOI.

epithermal (0.1 eV–100 keV) [18], thermal (around 25 meV) [19], and cold (around 1 meV) [20] neutrons were generated by LDNS. Radiography imaging with laser-driven thermal neutrons was also reported [16]. In these studies, moderators were used to decelerate fast neutrons from the source. However, this scheme inevitably expands the duration of neutrons and causes reduction in energy resolution. Thus, one of the key techniques for LDNS applications is to develop an appropriate moderator to effectively generate the low-energy neutrons with a relatively short pulse duration.

In this paper, we report the acceleration mechanism of ions (protons and deuterons) with a ps pulse of a high-intensity laser, which enables sufficient generation of fast neutrons. We find the scaling model on the neutron yield, using the experimental measurements and the analytical prediction. By developing a miniature moderator to decelerate the fast neutrons, our LDNS provides epithermal neutrons with a short pulse duration and high fluence to perform a neutron spectroscopy with a beamline of a few meters. We demonstrate a single-shot detection of isotopes by using neutron resonance transmission analysis (NRTA) with a sufficient resolution.

II. ION ACCELERATION MECHANISM

The laser pulse with an intensity (I_L) of 10^{18}–10^{19} W cm^{-2} from the LFEX laser system [21] is focused onto a foil of deuterated polystyrene (CD) with a thickness of 1.5 or 5 μm. (See Appendix A for the details of the laser parameters.) The plasma induced on the rear side of the CD foil serves as an ion source and simultaneously accelerates ions up to MeV energies. The accelerated ions then bombard a beryllium (Be) block (ϕ5-mm and 10-mm cylinder) that acts as a neutron source. Figure 1(a) shows the ion spectra analyzed in the target rear side, when the Be block is removed. (See Appendix B for the details of the ion analysis.) Here, protons (p), originating from the contaminant layer of oil and water on the CD surface, are accelerated up to 30 MeV at maximum. The deuterons (d), originating from the target material, are accelerated up to 7 MeV/u (14 MeV in total) at maximum. This feature is advantageous for neutron (n) generation. The ^{9}Be$(p,n)^9$B reaction, which is the dominant proton-induced reaction on Be in the MeV energy region, is endothermic, with a threshold energy of approximately 2 MeV; hence, the low-energy protons do not contribute to neutron generation. In contrast, the ^{9}Be(d,xn) reaction ($x = 1, 2, \ldots$) allows us to produce a softer spectrum of neutrons by using the low-energy deuterons, thanks to the reaction starting at a lower threshold energy compared to the ^{9}Be$(p,n)^9$B reaction [Fig. 2(d)].

Figures 1(b) and 1(c) show the results of the two-dimensional (2D) particle-in-cell (PIC) simulation using the PICLS code [22]. (See Appendix C for details.) In the earlier time stage [Fig. 1(b), $t = 0.3$ ps], the charge separation is induced by the hot electrons, and an electric field is formed. The electric field accelerates the protons, which have the largest charge-to-mass ratio, $q/M = 1$. This mechanism is well known as target normal sheath acceleration (TNSA) [25], where the sheath at the expanding ion front plays an important role [26–28]. We call this the "first sheath." However, the deuterons ($q/M = 1/2$) are not accelerated by the first sheath. In the later stage [Fig. 1(c), $t = 0.833$ ps], the first sheath depletes protons from the rear surface. Consequently, the charge neutrality is broken around the proton tail (seen around $x = 35$ μm), and additional charge separation and an electric field are induced between the proton tail and the bulk plasma. This electric field, hence termed "second sheath," accelerates deuterons that were initially covered by the contaminant layer.

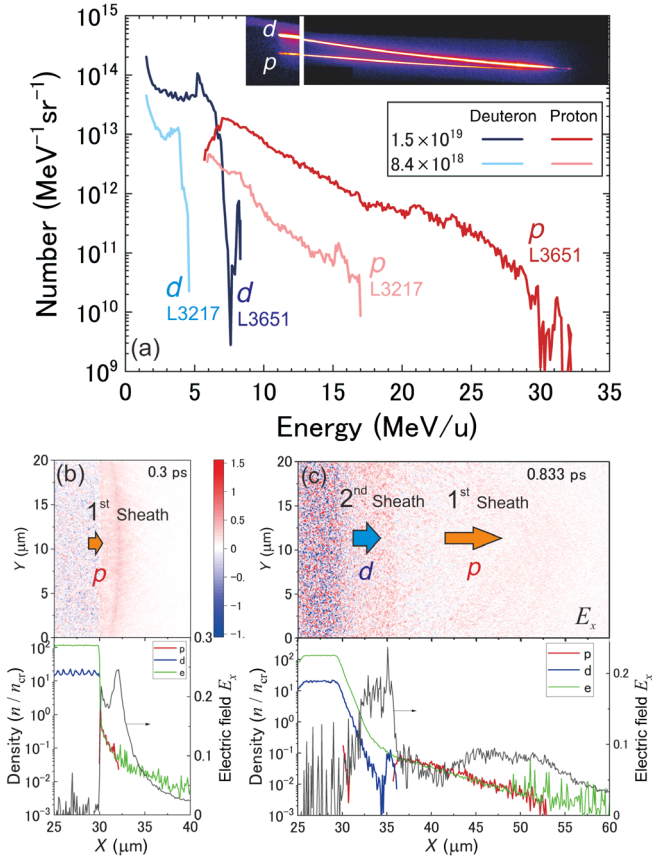

FIG. 1. (a) Energy distribution of protons (p) and deuterons (d) measured with the Thomson parabola ion spectrometer (TP) for two different laser intensities: 1.5×10^{19} and 8.1×10^{18} W cm^{-2}. The laser shot number is also displayed. The inset shows the raw data of parabolic curves for the shot L3651. (b) and (c) Results of the 2D PIC simulation with the PICLS code [22], showing the electric fields induced on the rear side of the foil at 0.3 ps (b) and 0.833 ps (c) after the laser incidence. The initial position of the foil rear surface is at $x = 30$ μm, and the center axis of the laser is at $y = 10$ μm in the upper figures. The lower figures show the electric fields integrated over the y axis as the black line, together with the densities of protons, deuterons, and electrons.

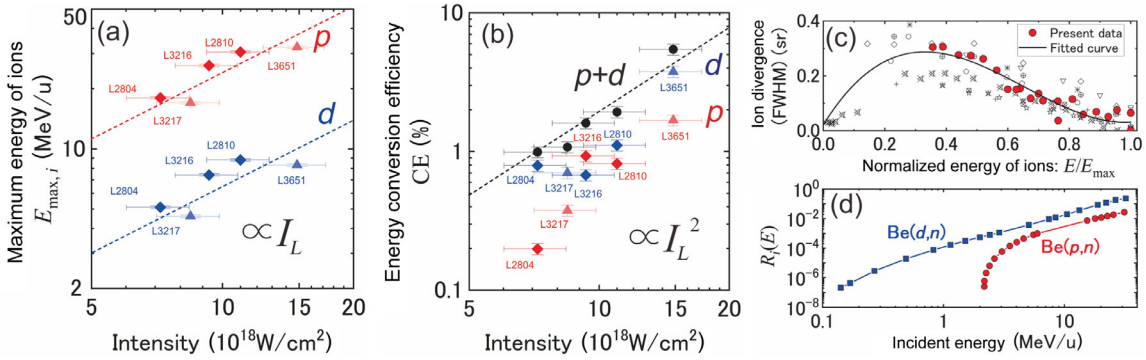

FIG. 2. (a) and (b) Experimental results of the maximum energy of ions ($E_{\mathrm{max},i}$) (a) and the energy conversion efficiencies (CE) from the laser to ions (b) as a function of the laser intensity for protons (red) and deuterons (blue). The results are measured with target foils of 1 and 5 μm (triangles) and 5 μm (rhombus) in thickness, respectively. The total CE for the protons and deuterons are shown as black circles in panel (b). The CE values are evaluated by using the total kinetic energy of the ions K [Eq. (5)] divided by the laser energy. (c) Divergence angle of ions measured as a function of the energy normalized by the maximum ion energy. The black symbols show results of previous works [23]. (d) Number of neutrons generated per one ion incident to sufficiently thick, solid Be blocks [24].

The acceleration of multi-ion species from the expanding plasma [29–32] reveals that the distinct rates of expansion of the different ion species play a role in the formation of the ion acceleration field. We find that the encounter between the ion clouds of different species affects the energy spectra of the ions. In Fig. 1(c), one can see a hump of deuteron density at $x = 35$ μm, attributed to the kick-back by the lowest-energy protons. This leads to the quasimonoenergetic peak at the high-energy region of the deuteron spectra shown in Fig. 1(a).

We find that the maximum energy of ions ($E_{\mathrm{max},i}$) [Fig. 2(a)] and the energy conversion efficiency (CE) from the laser into ions [Fig. 2(b)] are scaled by the laser intensity according to I_L and I_L^2, respectively. The survey of data [33–36] demonstrates that the maximum energy of accelerated protons increases as I_L for relatively short laser pulses (40–150 fs) and as $I_L^{1/2}$ for longer pulse durations (0.3–1 ps). Recently, a multivariate scaling model [37] developed with Bayesian influence reported that the proton energy increases as I_L, attributed to the increase of the temperature and the density of hot electrons. In the region of a ps timescale, it was theoretically found [38] that the laser-induced plasma laterally confined around the laser focal spot enhanced the hot electron temperature and density, and these enhancements can result in an increase of the proton energy steeper than $I_L^{1/2}$. The present study experimentally demonstrates the I_L dependency [Fig. 2(a)] of the ion energies for the long pulse duration (1.5 ps) due to the effect of the hot electron confinement, which is the benefit of the large focal spot [27]. In the previous study [34], it was experimentally found that the CE of protons increases as I_L^2 in the range of $I_L = 0.7$–6×10^{19} W cm^{-2}, being consistent with the present experimental result. For higher intensities, the CE shows a weaker dependency: CE $\propto I_L$ [39] for $I_L \sim 10^{20}$ W cm^{-2}. These findings determine the validity and limitations of the I_L^4 dependency of the neutron yield discussed in the next section.

III. NEUTRON GENERATION AND SCALING MODEL

The neutron generation is examined by putting the Be block back on the downstream of the CD foil [seen in Fig. 3(a)]. The neutrons are measured by stacks of CR-39 solid-state nuclear track detectors (sensitive for 1–10 MeV neutrons) surrounding the Be target. (See Appendix D for the calibration of the CR-39.) The neutron energy spectrum [Fig. 3(c)] measured by a time-of-flight (TOF) detector for fast neutrons [15] shows that more than 90% of the neutrons have energies below 10 MeV. Note that the TOF detector was calibrated by a bubble detector spectroscopy [40] and an activation method with $(n, 2n)$ nuclear reactions [15]. Although the angular distributions of the neutrons [Fig. 3(b)] are close to isotropy, it shows a greater tendency toward the forward direction (0°). Figure 4 shows the yield of the fast neutrons (triangles) measured by the CR-39 detectors in the forward (close to 0°) and perpendicular (close to 90°) directions as a function of the laser intensity I_L. The neutron yield $Y = 2.3 \times 10^{10}$ sr^{-1}, corresponding to $2 - 3 \times 10^{11}$ neutrons of 1–10 MeV in 4π, is experimentally obtained with $I_L = 1.1 \times 10^{19}$ W cm^{-2}. Here, we find that the neutron yield rapidly increases according to I_L^4.

The neutron yield Y [sr^{-1}] is written as

$$Y = \frac{1}{4\pi} \sum_{i=p,d} \int_0^{E_{\mathrm{max},i}} \frac{dN_i}{dE} R_i(E) dE. \tag{1}$$

Here, $(dN_i/dE) = (dN_i/dEd\Omega)\Omega(E/E_{\mathrm{max},i})$ is the energy distribution for the protons ($i = p$) or the deuterons ($i = d$).

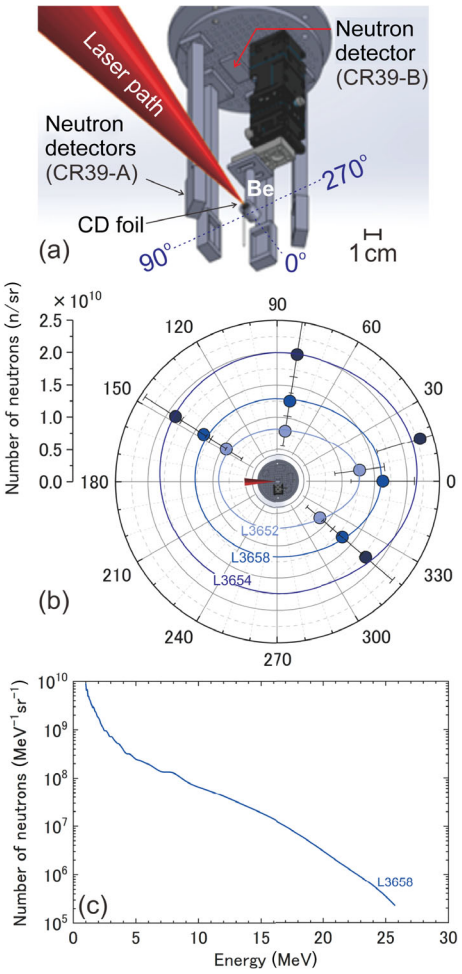

FIG. 3. (a) Setup of the LDNS and neutron detectors placed in the horizontal plane (CR39-A) and the vertical direction (CR39-B) of the LDNS. (b) Angular distributions of the neutrons measured by the CR39-A detectors for three different laser shots. The neutron yields of around 0° and 90° are used for the scaling in Fig. 4. (c) Energy distribution of the fast neutrons in the MeV range measured by the TOF detector [15].

Note that $dN_i/dEd\Omega$ is the differential energy distribution of the ions in the direction of the ion analyzer [Fig. 1(a)], and $\Omega(E/E_{\max,i})$ is the function of angular divergence depending on the ion energy [Fig. 2(c)]. Additionally, $R_i(E)$ [Fig. 2(d)] is the neutron generation rate [24] when one ion is incident to a sufficiently thick Be target [Fig. 2(d)].

We predict the neutron yield from Eq. (1) by using our experimental data on ions: $E_{\max,i}$ [Fig. 2(a)]; $dN_i/dEd\Omega$ [Fig. 1(b)], measured by the ion analyzer; and $\Omega(E/E_{\max,i})$ [Fig. 2(c)]. The results displayed as the open triangles in Fig. 4 demonstrate good agreement with the trend of experimentally measured neutron yields. This calculation supports the idea that our model [Eq. (1)] can predict the neutron yields from the spectra of the primary ions. The neutron yields calculated from the protons and deuterons

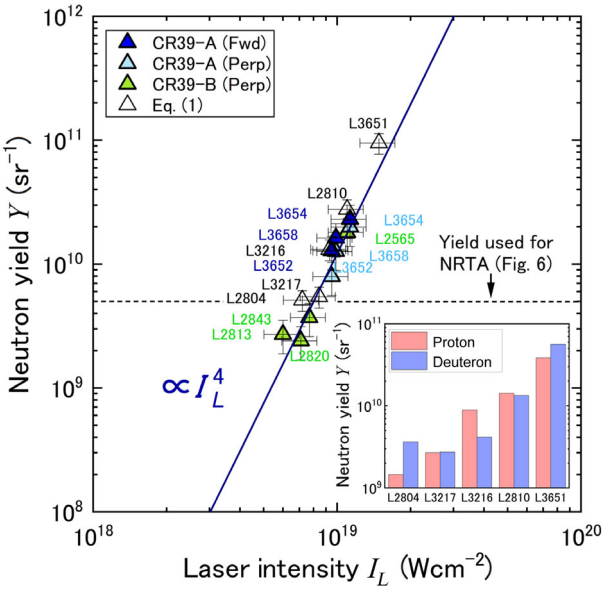

FIG. 4. Neutron yield Y per steradian as a function of the laser intensity I_L. The present results are shown as the colored triangles: dark blue by the CR39-A close to 0°, sky blue by the CR39-A close to 90°, and green by the CR39-B. The open triangles show the yields evaluated from the data of the ions in Figs. 1 and 2. The inset shows the contribution to the neutron generation by protons (red) and deuterons (blue) evaluated from the ion data by using the scaling model [Eq. (3)].

are shown separately in the inset, where the contribution of the deuterons roughly reaches 50% of the total.

We aim to elucidate the theoretical background of the I_L^4 dependency of the neutron yield. In Eq. (1), $R_i(E)$ increases with the square of the ion energy E^2 in the higher energy range. Hence, we can write

$$Y \propto \sum_{i=p,d} \int_0^{E_{\max,i}} \frac{dN_i}{dE} E^2 dE \tag{2}$$

and

$$\frac{dY}{dE_{\max,i}} \propto \sum_{i=p,d} \frac{dN_i}{dE} E^2 \Big|_{E=E_{\max,i}}. \tag{3}$$

Assuming that the maximum ion energy $E_{\max,i}$ increases as I_L^k, we obtain $dE_{\max,i}/dI_L \propto I_L^{k-1}$, where k is a scaling parameter discussed later. Then, we obtain

$$\frac{dY}{dI_L} = \frac{dY}{dE_{\max,i}} \frac{dE_{\max,i}}{dI_L} \propto I_L^{k-1} \sum_{i=p,d} \frac{dN_i}{dE} E^2 \Big|_{E=E_{\max,i}}. \tag{4}$$

The conversion efficiency from the laser energy to the total ion energy is written as $\mathrm{CE} = K/\mathcal{E}_L$, where K is the total kinetic energy of the ions, and $\mathcal{E}_L$ is the incident laser

energy proportional to I_L. Assuming CE $\propto I_L^m$, the total ion energy can be expressed by

$$K = \mathrm{CE}\mathcal{E}_L = \sum_{i=p,d} \int_0^{E_{\max,i}} \frac{dN_i}{dE} E dE \propto I_L^{m+1}, \quad (5)$$

where m is the scaling parameter for CE discussed later. Therefore, we obtain

$$\frac{dK}{dI_L} = \frac{dK}{dE_{\max,i}} \frac{dE_{\max,i}}{dI_L} \propto I_L^{k-1} \sum_{i=p,d} \frac{dN_i}{dE} E \Big|_{E=E_{\max,i}} \propto I_L^m. \quad (6)$$

Considering the ratio between Eqs. (4) and (6), we obtain

$$\frac{dY}{dI_L} / \frac{dK}{dI_L} \propto E_{\max,i} \propto I_L^k. \quad (7)$$

Then, $dY/dI_L \propto I_L^{k+m}$. Therefore, we reach the scaling law on the neutron yield as follows:

$$Y \propto I_L^{k+m+1}. \quad (8)$$

The I_L^4 increase in the present study is consistently explained by $k = 1$ ($E_{\max,i} \propto I_L$) and $m = 2$ (CE $\propto I_L^2$), as demonstrated in Figs. 2(a) and 2(b).

As discussed in the previous section, the parameters k and m depend on the laser-plasma interactions, varying in the ranges of $k = 0.5$–1 and $m = 1$–2 within the scheme of TNSA. The ion scaling [33–36] indicates $E_{\max,p} \propto I_L^{1/2}$ for longer pulse durations (0.3–1 ps), when the efficient confinement of the electrons found in this study is not involved. The CE increases as CE $\propto I_L^2$ for $I_L = 0.7$–6×10^{19} W cm^{-2} with 320-fs pulses [34] and CE $\propto I_L$ [39] for $I_L \sim 10^{20}$ W cm^{-2} with 1-ps pulses. Then, the neutron scaling shows $Y \propto I_L^{3.5}$ for the lower intensity region, and $Y \propto I_L^{2.5}$ for $I_L \sim 10^{20}$ W cm^{-2}. On the other hand, for fs pulse lasers, one can find $E_{\max,p} \propto I_L$ [33–36]. However, the scaling on the CE is not yet clarified for the fs pulses. A further comprehensive survey is required.

IV. NEUTRON RESONANCE ABSORPTION SPECTROSCOPY

Epi-thermal and thermal neutrons are used for broader applications rather than fast neutrons. Here, we demonstrate that a single-shot NRTA is realized by the LDNS. NRTA is based on the nuclear resonance absorption process, where a neutron is efficiently captured at the resonance energy of a nucleus in the energy region of eV. The resonance energy depends on the nuclear species. The resonance structure is often analyzed by a TOF method. In a simple expression, the neutron energy E_n is given by $E_n = m(D/\tau)^2/2$ for a time of flight τ, a flight distance D, and neutron mass m. Then, the energy resolution ΔE_n is determined by

$$\Delta E_n / E_n = 2\Delta\tau\sqrt{2E_n/m}/D, \quad (9)$$

where reducing the temporal spread $\Delta\tau$ linearly shortens the distance D.

A promising way to obtain lower-energy neutrons is by installing moderation mediums [18–20] close to the LDNSs. However, it causes an issue that the pulse (0.1–1 ns) of fast neutrons is broadened during the moderation process. To solve this issue, we develop a miniature moderator directly surrounding the LDNS. In general, the temporal duration of moderated neutrons becomes shorter as the moderator thickness is reduced; consequently, the neutron number decreases unfavorably for applications. This is because the neutron moderation is a statistical process involving multiple elastic collisions. We calculate the duration and fluence (neutron number per unit area) of 10-eV energy neutrons at the exit of a moderator having a simplified structure with a thickness of L, shown in Fig. 5(c) by the PHITS Monte Carlo code [41]. Here, the fluence decreases rapidly for $L < 3$ cm, although the duration is reduced linearly. This result is reasonable considering that the mean free path for 1-MeV energy neutrons is around 2 cm. Hence, a balance point between the duration and fluence can be found around $L = 3$ cm. We examine this approach by using the experimental setup as shown in Fig. 5(a).

The fast neutrons from the Be block are moderated by a 3-cm-thick high-density polyethylene (HDP) [Fig. 5(b)]. The energy spectrum is measured by the TOF method with a ^{6}Li-doped scintillator (1 cm in thickness, 5 cm in diameter) connected to a time-gated photomultiplier tube (PMT) [43] to remove the x-ray flash induced by the laser-plasma interaction. The detector is attached with a cadmium collimator and shielded by walls of boron-doped polyethylene and lead. We place samples of silver (Ag), tantalum (Ta), and indium (In) with a thickness of 0.1 mm in the front of the detector. These materials exhibit many resonant peaks on the neutron absorption cross sections in the energy range of 1–100 eV [Fig. 5(d)]. Especially in the energy range of 3–5 eV, the peaks of ^{115}In, ^{181}Ta, and ^{109}Ag are adjacent to each other. We demonstrate the performance of our NRTA beamline by identifying these resonant peaks.

Figure 6(a) shows the TOF signal of the epithermal neutrons transmitted through the sample. The transmission ratio converted from the TOF signal is shown in Fig. 6(b). Three dips around 3–5 eV are identified on the neutron spectrum, attributed to the resonance absorptions of ^{115}In (3.81 eV), ^{181}Ta (4.28 eV), and ^{109}Ag (5.19 eV), which corresponds well to the cross sections for neutron capture processes shown in Fig. 5(d). The simulated result is

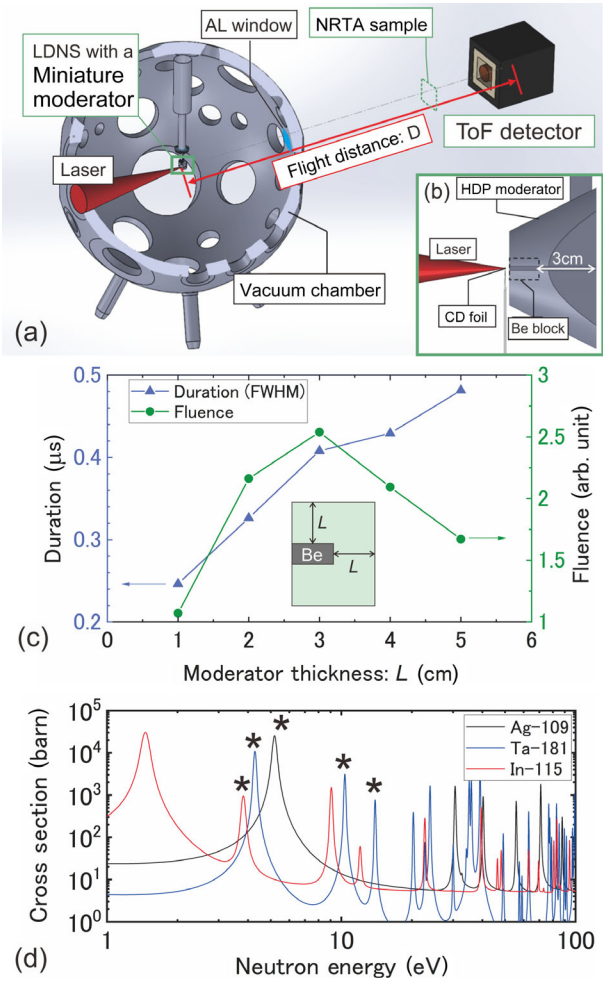

FIG. 5. (a,b) Schematic pictures of the NRTA beamline (a) and the miniature moderator (b) installed on the LDNS. (c) Simulated results of pulse duration and fluence of 10-eV neutrons at the exit of the moderator as a function of the moderator thickness. (d) Cross sections for neutron capture processes of ^{115}In, ^{181}Ta, and ^{109}Ag [42]. The marked peaks are analyzed in the experiment.

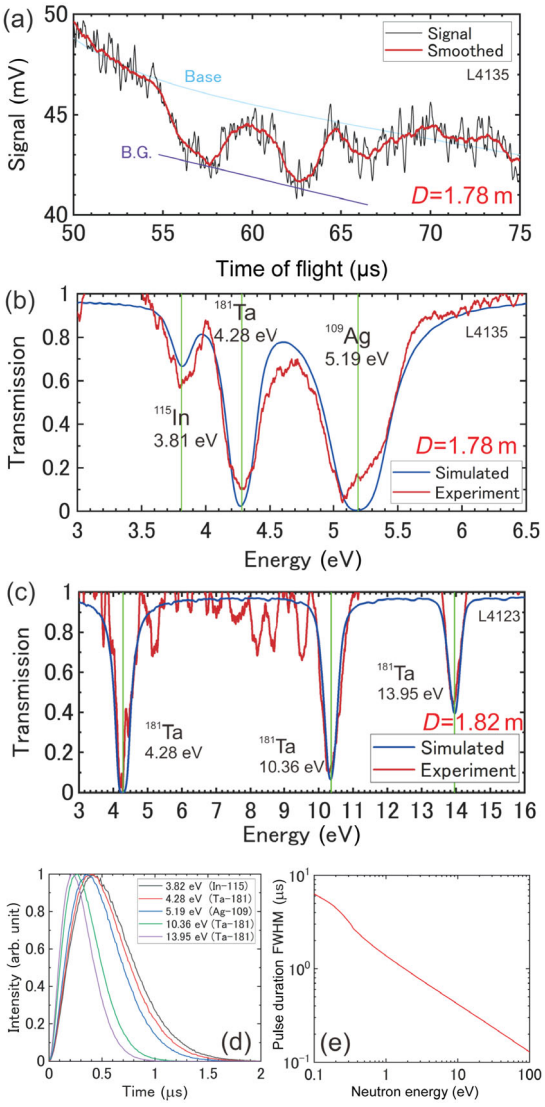

FIG. 6. (a) Signal measured by the TOF detector for the multilayer sample of 0.1-mm-thick Ag, Ta, and In. (b,c) Comparisons between experimental and simulated transmittances as a function of the neutron energy for the Ag-Ta-In multilayer (b) and the 0.5-mm-thick Ta (c). (d,e) Pulse duration calculated at the exit of the moderator [Fig. 5(b)] for the neutrons having ±1% energy spread.

obtained by the PHITS code when we use the experimental results on the fast neutrons [Figs. 3(b) and 3(c)] as input data and assume the geometries of the experimental setup. The three dips due to the resonant absorptions of ^{115}In, ^{181}Ta, and ^{109}Ag are clearly reproduced. Figure 6(c) shows the NRTA result for a thicker sample, a Ta foil with 0.5-mm thickness, where the resonances of ^{181}Ta are measured at 4.28, 10.36, and 13.95 eV, in agreement with the simulation.

The estimated energy resolution is $\Delta E_n/E_n = 2.3\%$ at $E_n = 5.19 \pm 0.05$ eV with the flight distance $D = 1.78$ m, according to Eq. (9). Here, the time spread is given by $\Delta\tau = \sqrt{\Delta\tau_m^2 + \Delta\tau_d^2}$, where $\Delta\tau_m = 581$ ns (FWHM) and $\Delta\tau_d = 312$ ns (FWHM) are the spread due to the moderation of neutrons [Fig. 6(d)] and the time fluctuation of the detector, respectively. The obtained resolution enables the analysis of multilayer samples, where the resonance energies are adjacent to each other. The NRTA analysis is performed with a single laser shot. Using the I_L^4 law, we estimate the yield of fast neutrons to be approximately 5×10^9 sr^{-1} with $I_L = 8 \times 10^{18}$ W cm^{-2}. Using the PHITS code, we evaluate the epithermal neutron fluence for $1 \le E_n \le 20$ eV to be approximately 1×10^2 cm^{-2} on the TOF detector surface. This fact suggests that the single-shot analysis can be performed at several facilities [11–14] that achieved the neutron yield of about 10^9 sr^{-1} (about 10^{10} in the 4π direction) at the secondary target.

V. DISCUSSION AND FUTURE PROSPECTS

The neutron resonance spectroscopy has been widely performed at accelerator-based neutron facilities, including n_TOF at CERN [44], NOBORU at J-PARC [45], GELINA at EC-JRC Geel [46], KENS [47] at KEK, and HUNS at Hokkaido University [48]. In GELINA, the flux of 1–20 eV neutrons at a sample position 10–20 m from the neutron source is typically about 10^3 cm^{-2} s^{-1} [46] with 800 Hz. The acquisition of the neutron resonance spectrum is preformed by time integration typically over 0.5–5 hours [49] at the accelerators. Even though the accelerator-based neutron sources are stable for several hours, the time acquisition increases systematic errors. On the other hand, the LDNS delivers 10^2–10^3 cm^{-2} neutrons of 1–20 eV (see Sec. IV) on the sample within the sub-μs duration, allowing the NRTA measurement without time acquisition. This is the predominant factor that distinguishes the LDNS from accelerator-based neutron facilities.

The short acquisition time (sub-μs) brings temporal resolution to the neutron resonance spectroscopy for the first time. In general, the resonance absorption dips measured on the spectrum are broadened by the Doppler effect caused by the thermal vibration of the sample nuclei. The Doppler broadening is utilized for a remote thermometry in accelerator facilities [50,51], where the data acquisition is performed by time integration over a few hours. LDNS may allow one to complicate the remote thermometry by a single shot. In particular, we have succeeded in identifying In, which is one of the indispensable materials for modern devices, including blue-light-emitting diodes and semiconductor power devices. This fact implies the possibility of real-time temperature monitoring for these devices *in operation*.

We discuss the possible improvements and conceptual limitations of the present laser-driven NRTA. We demonstrate the energy resolution $\Delta E_n/E_n = 2.3\%$ for $E_n = 5.19$ eV with the flight distance $D = 1.78$ m, as discussed in the previous section. Here, the energy resolution is comparable to that of accelerator facilities, for instance, $\Delta E_n/E_n = 1\%$ for 1 eV, which is deduced by Eq. (9) using the temporal spread at the moderator $\Delta\tau_m = 2.9$ μs (FWHM) and the flight distance $D = 14$ m reported in Ref. [45]. The energy resolution can, in principle, be improved linearly by expanding the flight path length D. Figure 7 shows the $\Delta E_n/E_n$ at $E_n = 5.2$ eV as a function of D with the present configuration of the moderator. On the other hand, as a zero-order approximation, the neutron density on a detector decreases as D^{-2}. This indicates that the neutron yield from the source Y required for the single-shot NRTA increases as D^2. In Fig. 7, we plot the D^2 dependency of the required neutron yield with the red line, which crosses the present experiment length of $D = 1.8$ m at the point $Y = 5 \times 10^9$ sr^{-1}. By expanding the flight path to $D = 18$ m, the energy resolution is improved to

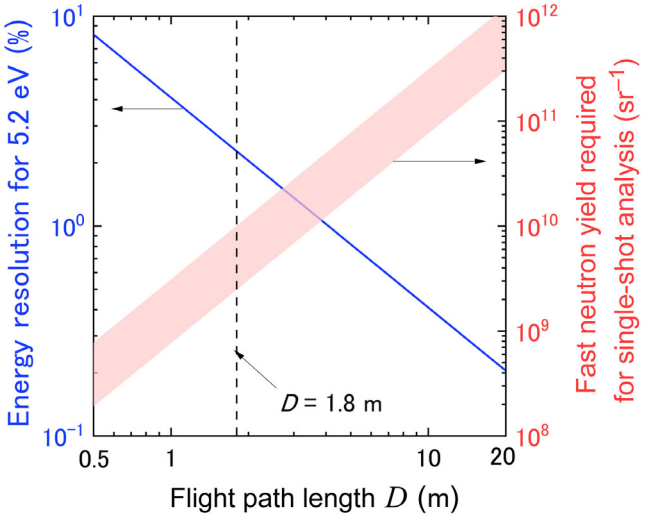

FIG. 7. Blue: energy resolution of NRTA $\Delta E_n/E_n$ at $E_n = 5.2$ eV estimated by Eq. (9) as a function of the flight path length D for the configuration of the present moderator. Red: fast neutron yield at the source to achieve the single-shot analysis.

$\Delta E_n/E_n = 0.23\%$ for 5.2 eV, when the single-shot analysis can be performed with $Y = 10^{11}$ sr^{-1}, which is the upper achievable limit of this study (Fig. 4).

Another possible direction of study is exploring extremely short flight paths. In the case of $D = 0.5$ m, the resolution is given by $\Delta E_n/E_n = 8\%$, which is close to the resonance width of ^{181}Ta [Fig. 5(d)], implying the limit for identifying elements or isotopes. Realizing the short flight path allows the NRTA beamline to be installed in places where it has not been possible before, such as factories and nuclear fuel storage facilities.

Finally, we discuss the possibility of extending the NRTA configuration to more compact and higher repetition-rate laser systems. By using the scaling model, we can predict the yield of fast neutrons from the experimental energy spectrum of ions. In a recent study [52], the laser pulse of 18 J, 5×10^{21} W cm^{-2} accelerated about 10^{10} MeV^{-1} sr^{-1} protons up to 60 MeV. By locating a 2-cm-thick Be block behind the primary target, we stop all the protons inside the Be, and the neutron generation rate $R_i(E)$ shown in Fig. 2(d) is available. According to Eq. (3), we can obtain the fast neutron yield of 10^8 n/sr/shot [53], approaching 1 order of magnitude below the yield used for the present NRTA (10^9 n/sr/shot on the Be). The generated neutrons, expected to have a broad energy up to the maximum energy of the protons (60 MeV), are moderated down to the epithermal region with sufficient fluence by a 3-cm-thick moderator (see Appendix E). The neutron yield can be enhanced by the emerging laser system at the ELI-NP facility [54], which delivers 200 J pulses with 0.017 Hz, enabling the single-shot NRTA with high-repetition rate. The upcoming lasers operating with 10–100 Hz [55–57] will further improve the repetition rate of the LDNS systems.

VI. CONCLUSION

We have demonstrated the single-shot NRTA with the LDNS. Based on the comprehensive studies on laser-driven ion acceleration and neutron generation, we discovered the novel scaling model that predicts the fast neutron yield from the ion spectrum, indicating the fourth power dependency on the laser intensity. Installing the adequate neutron moderator on the LDNS, we developed the 1.8-m beamline for NRTA with an energy resolution of 2.3% for 5.19 ± 0.05 eV, which is sufficient to analyze elements or isotopes. One NRTA spectrum was obtained with a single pulse of neutrons generated by a single laser shot. We discussed the possibilities of the laser-driven NRTA and the direction of future developments based on the experimental findings to achieve the single-shot analysis. The key to realize the laser-driven NRTA system is to explore the ultimate possibilities of LDNS that offer an advantage over conventional neutron sources for their high brilliance, compactness, and cost effectiveness. Through this activity, the LDNS will give us a wide range of opportunities that bring the high-temporal resolution beam of neutrons into fields that have never benefited from the technology of neutron science.

ACKNOWLEDGMENTS

This work was funded by Grant-in-Aid for Scientific Research (No. 25420911, No. 26246043, and No. 22H02007) of MEXT, A-STEP (AS2721002c), and PRESTO (JPMJPR15PD) commissioned by JST. The authors thank the technical support staff of ILE for their assistance with the laser operation, target fabrication, and plasma diagnostics. This work was supported by the Collaboration Research Program of ILE, Osaka University. The collaboration of the J. A. E. A. was supported by the subsidy of the MEXT for nuclear security promotion. A. Y. deeply appreciates useful suggestions from Professor Kiyanagi of Nagoya University and Professors Kamiyama and Sato of Hokkaido University on the estimation of the neutron generation and moderation, Dr. M. Kanasaki and Professor K. Oda of Kobe University on the evaluation of neutron yield, and Professor I. Murata of Osaka University on the detector calibration using his Am-Be neutron source. A. Y. gratefully appreciates suggestions from the committee on "Laser-driven Neutron Source" commissioned by the Laser Society of Japan. A. Y. also appreciates fruitful discussions with the members of a consultancy meeting on "Advances in Laser-driven Neutron and X-ray Sources" commissioned by IAEA.

APPENDIX A: LASER PARAMETERS

We performed the experiment at the LFEX laser facility [21,58] of Osaka University. LFEX simultaneously delivers four laser beams (H1–H4). The maximum laser energy in total was up to 1 kJ (250 J for each beam) on the target. The laser wavelength was $\lambda = 1.053$ μm. The laser pulses were focused by an $F/10$ off-axis parabolic mirror (OAP). The focal spot diameter was $r_f = \phi 50$ μm (FWHM) for H1, H3, and H4 beams and $r_f = \phi 30$ μm (FWHM) for H2. We performed the laser intensity survey by varying the laser energy, when we set the pulse duration around 1.5 ps. We monitored the shot-by-shot energy and pulse duration of the laser. We measured the laser energy by detecting the leaked light of the laser behind the mirror at the position between the main amplifier of the LFEX system and the compressor and evaluated the on-target energy from the throughput ratio of the beams. The pulse duration was measured by a streak camera located behind the mirror just downstream of the compressor. The results are shown in Table I for each beam of the LFEX, H1–H4. For the lower intensity cases, we used only two (H2 and H4) of the four beams. The error bars on the laser intensity (Figs. 2 and 4) are predominantly attributed to the fluctuation of the laser focusing, which was not monitored for the high-power shots used for the experiment. We estimated the focusing fluctuation from the data of encircled energy

TABLE I. Results of shot-by-shot monitoring of the laser energy and pulse duration.

	Laser energy on target (J)					Pulse duration (FWHM) (ps)			
Shot no.	H1	H2	H3	H4	Total	H1	H2	H3	H4
L2565	168	206	180	205	760	1.35	1.24	0.93	1.92
L2810	0	226	0	223	449	···	1.06	···	1.50
L2804	0	194	0	189	383	···	1.72	···	1.91
L2820	0	196	0	194	389	···	1.35	···	1.58
L2831	0	246	0	247	493	···	1.13	···	1.27
L2843	0	209	0	215	424	···	1.07	···	1.30
L3216	0	209	0	199	408	···	1.22	···	1.28
L3217	0	205	0	193	398	···	1.30	···	1.40
L3651	240	235	223	233	931	1.19	1.39	1.67	1.41
L3652	244	235	226	227	932	2.06	2.06	2.16	2.70
L3654	240	233	216	217	906	1.61	1.75	1.90	1.97
L3658	235	210	205	204	854	1.92	1.74	2.11	2.16

obtained with low-power laser shots used for the laser focusing adjustment. As a result, the encircled energy changed with a standard deviation of $\sigma = 8.2\%$. We used the error bar of $2\sigma = 16.4\%$ for the laser intensity.

APPENDIX B: ANALYSIS OF LASER-ACCELERATED IONS

The ion energy spectra were observed using a Thomson parabola (TP) spectrometer, when the Be block was moved away. The TP employs a permanent dipole magnet (0.85 T) and a pair of copper electrodes (12.5 kV/cm). The detailed setup is shown in Ref. [59]. An image plate (IP), BAS-TR2025/Fuji Film, was used as an ion detection device in the TP. On the TP analysis, ions having the same value of charge-to-mass ratio q/M are measured as the same parabolic curve, as shown in the inset of Fig. 1(b). Thus, the C^{6+} and O^{8+} ions, which can be accelerated from the target, are not distinguished from the deuterons. In order to avoid this, we placed aluminum (Al) foils having appropriate thickness on the IP and blocked the heavier ions. In the inset of Fig. 1(a), the right part of the IP is covered with an Al foil of 300 μm thickness, and the left part is covered with a 100-μm-thick Al foil. The energy of protons and deuterons after penetrating the Al covers was evaluated by the PHITS [41] code. The IP signals were converted into the energy spectra of deuterons and protons by using the calibration results in Refs. [60,61]. The lower limits of the energy detection are 1.4 MeV/u and 5.7 MeV/u for deuterons and protons, respectively. The spatial divergence of ions [Fig. 2(c)] was measured with a stack of radiochromic films.

The error bars on the maximum ion energy $E_{\mathrm{max},i}$ [Fig. 2(a)] are attributed to the energy resolution of the TP ($2\sigma = 2.8\%$) [59,62]. The error for the energy conversion efficiency from lasers to ions (CE) is attributed to the ion angular distribution Ω [Fig. 2(c)] obtained by a fitting using the function $\Omega(E/E_{\mathrm{max},i}) = 1.87 * (E/E_{\mathrm{max},i})^3 - 3.67 * (E/E_{\mathrm{max},i})^2 + 1.81 * (E/E_{\mathrm{max},i}) + 0.0219$ (solid line) with a standard deviation of $\sigma_\Omega = 3.9\%$. Considering that $\mathrm{CE} \propto \Omega E_{\mathrm{max},i}^2$, the error for CE is $2\sigma_{\mathrm{CE}} = 9.6\%$ as shown in Fig. 2(b).

The errors evaluated for $E_{\mathrm{max},i}$ and CE affect the errors for the calculation of the neutron yield Y from Eq. (1) (open triangles in Fig. 4). Considering that $Y \propto I_L^{k+m+1} \propto E_{\mathrm{max},i} CEI_L$, we obtain the error bar of $2\sigma = 19\%$.

APPENDIX C: PARTICLE-IN-CELL SIMULATION

Fully relativistic two-dimensional PIC simulations were performed by the PICLS code [22], which incorporates the Coulomb collisions among charged particles and the dynamic ionizations. The size of the simulation box is 200 μm in the x axis and 20 μm in the y axis with a mesh size of 1/120 μm. We initially located a target of deuterated polystyrene (CD) at $25 \le x \le 30$ μm having an electron density of $120n_c$, where $n_c = m_e\epsilon_0(2\pi c/e\lambda)^2 \simeq 1.1 \times 10^{27}\lambda_{\mu\mathrm{m}}^{-2}$ [m^{-3}] is the critical density. Note that c, m_e, e, and ϵ_0 are the speed of light in vacuum, the mass of the electron, the elementary charge, and the electric permittivity in vacuum, respectively. Here, $\lambda = 1.05$ μm is the laser wavelength. On the rear side of the CD target, we put a layer of hydrogen with a thickness of 1/120 μm as the surface contaminants. On the front side, we put a preformed plasma [27], the density of which increases as $120n_c \exp(x - x_0)/l_{\mathrm{pre}}$, where $x_0 = 25$ μm and $l_{\mathrm{pre}} = 1$ μm is the scale length. The initial charge states of ions are 3+ for carbon, 1+ for deuterons, and 0 for protons. The initial temperatures of ions and electrons are $T_{i0} = T_{e0} = 0.1$ keV. The average numbers of superparticles per cell in the distribution region of the plasma, i.e., in the 1 μm length, are 1×10^2 and 1.4×10^3 for ions and electrons, respectively.

APPENDIX D: NEUTRON MEASUREMENTS AND SENSITIVITY CALIBRATION OF CR-39 DETECTORS

Stacks of three layers of CR-39 ion track detectors (10 mm × 20 mm, BARYOTRACK, Fukubi) are used to measure the neutron number. The CR-39 stacks are located at a distance of 3 cm from the Be block. The solid angle is 18 msr. To prevent contamination by protons or deuterons accelerated from the target, we put a Pb plate in front of the CR-39 stack and wrap them with 12.5-μm-thick aluminum foil. The CR-39 is damaged by protons knocked-on by neutrons and generates pits that are visualized after chemical etching by a KOH solution. Here, only the third layer of the CR-39 is analyzed for the neutron counting. The first and second layers work as a radiator, where neutrons scatter protons and some parts of the scattered protons are detected by the third CR-39. This method enhances the detection efficiency of neutrons, and at the same time, the efficiency shows moderate dependence on the neutron energy [63]. The third layers of the CR-39 stack are etched by the KOH solution (6 mol/L, 70 °C) for 5 hours. For the case of the highest neutron yield (2.3×10^{10} n/sr), we count 2401 pits with the microscope on an area of 0.00235 cm^2, corresponding to 2.55×10^5 pits/cm^2. We arbitrarily choose four positions on the CR-39 and average the counted number. The distance between the CR-39 and the LDNS (Be block) is 3 cm.

We calibrate the detection efficiency by using an Am-Be neutron source at the Quantum Reaction Engineering Laboratory of Osaka University. The Am-Be source generates neutrons having a continuous energy distribution [64], which is similar to that of our LDNS. The energy of neutrons from Am-Be sources is in the range of 2–10 MeV, and the spectral intensity increases with the decreasing energy [64]. The fast neutron intensity of the Am-Be source

is 4.5×10^6 n/s. We put CR-39 stacks at a distance of 5 cm from the source using the same package as those used in the laser experiment. After 4 hours of exposure, the neutron fluence reaches 5.3×10^9 n/sr, which is comparable to the yield of our LDNS (10^9–10^{10} n/sr). The CR-39 layers are etched together with the CR-39 plates used in the LDNS experiment to avoid any discrepancy from the different condition of the solution.

We obtain 1.03×10^{-4} pits/n as the detection efficiency for the MeV-energy neutrons in the calibration experiment. The CR-39 sensitivity is nearly constant with neutrons for 1–5 MeV and rapidly decreases for more than 10 MeV [65], varying within the range of ±30% for 1–10 MeV. In our study, the error on the neutron yield is predominantly attributed to the detection sensitivity, depending on the neutron energy, not to the statistical error on the pit counting. We use an error of ±30% on the neutron yields measured by the CR-39 detectors.

APPENDIX E: SIMULATION ON THE NEUTRON MODERATION

To analyze the epithermal neutron spectra, we simulate the neutron moderation processes using the PHITS Monte Carlo code [41]. We input the experimental energy spectrum and angular distributions of fast neutrons [Figs. 3(b) and 3(c)] at the position of the Be block. We assume the moderator structure used in the experiment [Fig. 5(b)] for the simulation of NRTA. Figure 8 shows the energy spectra (solid line) at the bottom of the moderator obtained for the present experimental condition, where the neutron number is normalized by the number of incident fast neutrons. The pulse duration of the neutrons [Figs. 6(d) and 6(e)] at this position is also provided.

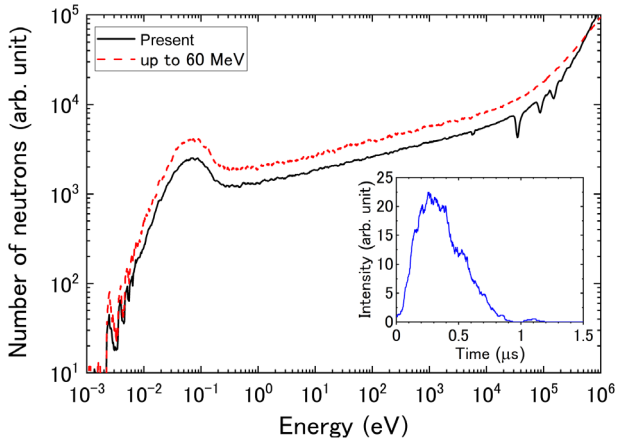

FIG. 8. Energy spectra of neutrons at the bottom (exit) of the moderator simulated using PHITS for the present experiment (solid line) and for the high-repetition laser system (dashed line) discussed in Sec. V. The inset shows the pulse duration of 10-eV neutrons obtained with the incidence of 60-MeV neutrons.

As described in Sec. IV, we evaluate the number of epithermal neutrons ranging from 1 to 20 eV to be about 1×10^2 cm^{-2} on the detector located 1.8 m downstream from the moderator. This neutron density corresponds to 3×10^6 sr^{-1} for 1–20 eV. Considering that the fast neutron number is 5×10^9 sr^{-1}, the moderation efficiency is 0.06% for the energy range of 1–20 eV.

We also show the energy spectrum (dashed line) predicted for the use of the high-repetition laser system discussed in Sec. V. By the simultaneous measurement of laser-driven ions and neutrons [16], we find that the maximum energy and the characteristic temperature of neutrons are in agreement with those of ions, respectively. Hence, in the PHITS simulation, we use the spectrum of fast neutrons derived from the proton spectrum of Ref. [52], having a maximum energy of 60 MeV. We find that the number of epithermal neutrons is comparable in the experiment and simulation. Additionally, the pulse duration of 10-eV neutrons (inset) obtained by the incidence of 60-MeV neutrons is as short as the present result [Fig. 6(d)].

[1] E. L. Clark, K. Krushelnick, M. Zepf, F. N. Beg, M. Tatarakis, A. Machacek, M. I. K. Santala, I. Watts, P. A. Norreys, and A. E. Dangor, *Energetic Heavy-Ion and Proton Generation from Ultraintense Laser-Plasma Interactions with Solids*, Phys. Rev. Lett. **85**, 1654 (2000).

[2] S. P. Hatchett *et al.*, *Electron, Photon, and Ion Beams from the Relativistic Interaction of Petawatt Laser Pulses with Solid Targets*, Phys. Plasmas **7**, 2076 (2000).

[3] A. Maksimchuk, S. Gu, K. Flippo, and D. Umstadter, *Forward Ion Acceleration in Thin Films Driven by a High-Intensity Laser*, Phys. Rev. Lett. **84**, 4108 (2000).

[4] P. A. Norreys, A. P. Fews, F. N. Beg, A. R. Bell, A. E. Dangor, P. Lee, M. B. Nelson, H. Schmidt, M. Tatarakis, and M. D. Cable, *Neutron Production from Picosecond Laser Irradiation of Deuterated Targets at Intensities of* 10^{19} W cm^{-2}, Plasma Phys. Controlled Fusion **40**, 175 (1998).

[5] L. Disdier, J. P. Garçonnet, G. Malka, and J. L. Miquel, *Fast Neutron Emission from a High-Energy Ion Beam Produced by a High-Intensity Subpicosecond Laser Pulse*, Phys. Rev. Lett. **82**, 1454 (1999).

[6] T. Ditmire, J. Zweiback, V. P. Yanovsky, T. E. Cowan, G. Hays, and K. B. Wharton, *Nuclear Fusion from Explosions of Femtosecond Laser-Heated Deuterium Clusters*, Nature (London) **398**, 489 (1999).

[7] K. L. Lancaster *et al.*, *Characterization of* ^{7}Li$(p,n)^7$Be *Neutron Yields from Laser Produced Ion Beams for Fast Neutron Radiography*, Phys. Plasmas **11**, 3404 (2004).

[8] A. Youssef, R. Kodama, H. Habara, K. A. Tanaka, Y. Sentoku, M. Tampo, and Y. Toyama, *Broad-Range Neutron Spectra Identification in Ultraintense Laser Interactions with Carbon-Deuterated Plasma*, Phys. Plasmas **12**, 110703 (2005).

[9] D. P. Higginson *et al.*, *Laser Generated Neutron Source for Neutron Resonance Spectroscopy*, Phys. Plasmas **17**, 100701 (2010).

[10] D. P. Higginson *et al.*, *Production of Neutrons up to 18 MeV in High-Intensity, Short-Pulse Laser Matter Interactions*, Phys. Plasmas **18**, 100703 (2011).

[11] M. Roth *et al.*, *Bright Laser-Driven Neutron Source Based on the Relativistic Transparency of Solids*, Phys. Rev. Lett. **110**, 044802 (2013).

[12] S. Kar *et al.*, *Beamed Neutron Emission Driven by Laser Accelerated Light Ions*, New J. Phys. **18**, 053002 (2016).

[13] A. Alejo *et al.*, *High Flux, Beamed Neutron Sources Employing Deuteron-Rich Ion Beams from* D_2O*-Ice Layered Targets*, Plasma Phys. Controlled Fusion **59**, 064004 (2017).

[14] A. Kleinschmidt *et al.*, *Intense, Directed Neutron Beams from a Laser-Driven Neutron Source at PHELIX*, Phys. Plasmas **25**, 053101 (2018).

[15] T. Mori *et al.*, *Direct Evaluation of High Neutron Density Environment Using* $(n, 2n)$ *Reaction Induced by Laser-Driven Neutron Source*, Phys. Rev. C **104**, 015808 (2021).

[16] A. Yogo *et al.*, *Single Shot Radiography by a Bright Source of Laser-Driven Thermal Neutrons and X-rays*, Appl. Phys. Express **14**, 106001 (2021).

[17] I. Pomerantz *et al.*, *Ultrashort Pulsed Neutron Source*, Phys. Rev. Lett. **113**, 184801 (2014).

[18] S. R. Mirfayzi *et al.*, *Experimental Demonstration of a Compact Epithermal Neutron Source Based on a High Power Laser*, Appl. Phys. Lett. **111**, 044101 (2017).

[19] S. R. Mirfayzi *et al.*, *A Miniature Thermal Neutron Source Using High Power Lasers*, Appl. Phys. Lett. **116**, 174102 (2020).

[20] S. R. Mirfayzi *et al.*, *Proof-of-Principle Experiment for Laser-Driven Cold Neutron Source*, Sci. Rep. **10**, 20157 (2020).

[21] J. Kawanaka *et al.*, *3.1-kJ Chirped-Pulse Power Amplification in the LFEX Laser*, J. Phys. **112**, 032006 (2008).

[22] Y. Sentoku and A. J. Kemp, *Numerical Methods for Particle Simulations at Extreme Densities and Temperatures: Weighted Particles, Relativistic Collisions and Reduced Currents*, J. Comput. Phys. **227**, 6846 (2008).

[23] P. R. Bolton *et al.*, *Instrumentation for Diagnostics and Control of Laser-Accelerated Proton (Ion) Beams*, Phys. Med. **30**, 255 (2014).

[24] I. S. Anderson, C. Andreani, J. M. Carpenter, G. Festa, G. Gorini, C.-K. Loong, and R. Senesi, *Research Opportunities with Compact Accelerator-Driven Neutron Sources*, Phys. Rep. **654**, 1 (2016).

[25] S. C. Wilks, A. B. Langdon, T. E. Cowan, M. Roth, M. Singh, S. Hatchett, M. H. Key, D. Pennington, A. MacKinnon, and R. A. Snavely, *Energetic Proton Generation in Ultra-intense Laser-Solid Interactions*, Phys. Plasmas **8**, 542 (2001).

[26] P. Mora, *Plasma Expansion into a Vacuum*, Phys. Rev. Lett. **90**, 185002 (2003).

[27] A. Yogo *et al.*, *Boosting Laser-Ion Acceleration with Multi-picosecond Pulses*, Sci. Rep. **7**, 42451 (2017).

[28] N. Iwata, K. Mima, Y. Sentoku, A. Yogo, H. Nagatomo, H. Nishimura, and H. Azechi, *Fast Ion Acceleration in a Foil Plasma Heated by a Multi-picosecond High Intensity Laser*, Phys. Plasmas **24**, 073111 (2017).

[29] S. Sakabe, T. Mochizuki, T. Yabe, K. Mima, and C. Yamanaka, *Velocity Distributions of Multi-ion Species in an Expanding Plasma Produced by a* 1.05-μm *Laser*, Phys. Rev. A **26**, 2159 (1982).

[30] V. T. Tikhonchuk, A. A. Andreev, S. G. Bochkarev, and V. Yu Bychenkov, *Ion Acceleration in Short-Laser-Pulse Interaction with Solid Foils*, Plasma Phys. Controlled Fusion **47**, B869 (2005).

[31] S. Ter-Avetisyan, M. Schnürer, P. V. Nickles, M. Kalashnikov, E. Risse, T. Sokollik, W. Sandner, A. Andreev, and V. Tikhonchuk, *Quasimonoenergetic Deuteron Bursts Produced by Ultraintense Laser Pulses*, Phys. Rev. Lett. **96**, 145006 (2006).

[32] G. G. Scott, D. C. Carroll, S. Astbury, R. J. Clarke, C. Hernandez-Gomez, M. King, A. Alejo, I. Y. Arteaga, R. J. Dance, A. Higginson *et al.*, *Dual Ion Species Plasma Expansion from Isotopically Layered Cryogenic Targets*, Phys. Rev. Lett. **120**, 204801 (2018).

[33] M. Borghesi *et al.*, *Laser-Driven Proton Acceleration: Source Optimization and Radiographic Applications*, Plasma Phys. Controlled Fusion **50**, 124040 (2008).

[34] J. Fuchs *et al.*, *Laser-Driven Proton Scaling Laws and New Paths Towards Energy Increase*, Nat. Phys. **2**, 48 (2006).

[35] A. Macchi, M. Borghesi, and M. Passoni, *Ion Acceleration by Superintense Laser-Plasma Interaction*, Rev. Mod. Phys. **85**, 751 (2013).

[36] H. Daido, M. Nishiuchi, and A. S. Pirozhkov, *Review of Laser-Driven Ion Sources and Their Applications*, Rep. Prog. Phys. **75**, 056401 (2012).

[37] Y. Takagi, N. Iwata, E. Humieres, and Y. Sentoku, *Multivariate Scaling of Maximum Proton Energy in Intense Laser Driven Ion Acceleration*, Phys. Rev. Res. **3**, 043140 (2021).

[38] N. Iwata, A. J. Kemp, S. C. Wilks, K. Mima, D. Mariscal, T. Ma, and Y. Sentoku, *Lateral Confinement of Fast Electrons and Its Impact on Laser Ion Acceleration*, Phys. Rev. Res. **3**, 023193 (2021).

[39] L. Robson *et al.*, *Scaling of Proton Acceleration Driven by Petawatt-Laser-Plasma Interactions*, Nat. Phys. **3**, 58 (2007).

[40] S. R. Mirfayzi *et al.*, *Calibration of Time of Flight Detectors Using Laser-Driven Neutron Source*, Rev. Sci. Instrum. **86**, 073308 (2015).

[41] T. Sato *et al.*, *Features of Particle and Heavy Ion Transport Code System (PHITS) Version 3.02*, J. Nucl. Sci. Technol. **55**, 684 (2018).

[42] K. Shibata *et al.*, *JENDL-4.0: A New Library for Nuclear Science and Engineering*, J. Nucl. Sci. Technol. **48**, 1 (2011).

[43] Y. Abe *et al.*, *Production of Intense, Pulsed, and Point-like Neutron Source from Deuterated Plastic Cavity by Monodirectional Kilo-Joule Laser Irradiation*, Appl. Phys. Lett. **111**, 233506 (2017).

[44] C. Guerrero *et al.*, *Performance of the Neutron Time-of-Flight Facility n_TOF at CERN*, Eur. Phys. J. A **49**, 27 (2013).

[45] H. Hasemi, M. Harada, T. Kai, T. Shinohara, M. Ooi, H. Sato, K. Kino, M. Segawa, T. Kamiyama, and Y. Kiyanagi,

Evaluation of Nuclide Density by Neutron Resonance Transmission at the NOBORU Instrument in J-PARC/MLF, Nucl. Instrum. Methods Phys. Res., Sect. A **773**, 137 (2015).

[46] B. Becker, S. Kopecky, H. Harada, and P. Schillebeeckx, *Measurement of the Direct Particle Transport through Stochastic Media Using Neutron Resonance Transmission Analysis*, Eur. Phys. J. Plus **129**, 58 (2014).

[47] T. Kamiyama, N. Miyamoto, S. Tomioka, and T. Kozaki, *Epithermal Neutron Tomography Using Compact Electron Linear Accelerator*, Nucl. Instrum. Methods Phys. Res., Sect. A **605**, 91 (2009).

[48] M. Furusawa *et al.*, *Activity of Hokkaido University Neutron Source HUNS*, Phys. Procedia **60**, 167 (2014).

[49] A. S. Tremsin *et al.*, *Neutron Resonance Transmission Spectroscopy with High Spatial and Energy Resolution at the J-PARC Pulsed Neutron Source*, Nucl. Instrum. Methods Phys. Res., Sect. A **746**, 47 (2014).

[50] T. Kamiyama, H. Noda, J. Ito, H. Iwasa, Y. Kiyanagi, and S. Ikeda, *Remote-Sensing, Non-destructive, and Computed-Tomography-Assisted Thermometry by Neutron Resonance Absorption Spectroscopy*, J. Neutron Res. **13**, 97 (2005).

[51] V. W. Yuan, J. D. Bowman, D. J. Funk, G. L. Morgan, R. L. Rabie, C. E. Ragan, J. P. Quintana, and H. L. Stacy, *Shock Temperature Measurement Using Neutron Resonance Spectroscopy*, Phys. Rev. Lett. **94**, 125504 (2005).

[52] T. Ziegler *et al.*, *Proton Beam Quality Enhancement by Spectral Phase Control of a PW-Class Laser System*, Sci. Rep. **11**, 1 (2021).

[53] In the spectrum [52], protons lower than 25 MeV are not shown. We evaluate the proton number by extrapolating the spectrum down to 5 MeV.

[54] K. A. Tanaka *et al.*, *Current Status and Highlights of the ELI-NP Research Program*, Matter Radiat. Extremes **5**, 024402 (2020).

[55] M. Divoký *et al.*, *150 J DPSSL Operating at 1.5 kW Level*, Opt. Lett. **46**, 5771 (2021).

[56] J. Ogino *et al.*, *10 J Operation of a Conductive-Cooled Yb:YAG Active-Mirror Amplifier and Prospects for 100 Hz Operation*, Opt. Lett. **46**, 621 (2021).

[57] J. Ogino *et al.*, *10-J, 100-Hz Conduction-Cooled Active-Mirror Laser*, Opt. Continuum **1**, 1270 (2022).

[58] Y. Arikawa *et al.*, *Ultrahigh-Contrast Kilojoule-Class Petawatt LFEX Laser Using a Plasma Mirror*, Appl. Opt. **55**, 6850 (2016).

[59] D. O. Golovin, S. R. Mirfayzi, S. Shokita, Y. Abe, Z. Lan, Y. Arikawa, A. Morace, T. A. Pikuz, and A. Yogo, *Calibration of Imaging Plates Sensitivity to High Energy Photons and Ions for Laser-Plasma Interaction Sources*, J. Instrum. **16**, T02005 (2021).

[60] A. Mančić, J. Fuchs, P. Antici, S. A. Gaillard, and P. Audebert, *Absolute Calibration of Photostimulable Image Plate Detectors Used as (0.5–20 MeV) High-Energy Proton Detectors*, Rev. Sci. Instrum. **79**, 073301 (2008).

[61] A. Alejo *et al.*, *Characterisation of Deuterium Spectra from Laser Driven Multi-species Sources by Employing Differentially Filtered Image Plate Detectors in Thomson Spectrometers*, Rev. Sci. Instrum. **85**, 093303 (2014).

[62] S. Tosaki *et al.*, *Evaluation of Laser-Driven Ion Energies for Fusion Fast-Ignition Research*, Prog. Theor. Exp. Phys. **2017**, 103J01 (2017).

[63] K. Oda, M. Ito, H. Miyake, M. Michijima, and J. Yamamoto, *Track Formation in CR-39 Detector Exposed to D-T Neutrons*, Nucl. Instrum. Methods Phys. Res., Sect. B **35**, 50 (1988).

[64] J. W. Marsh, D. J. Thomas, and M. Burke, *Am-Be and Am-B Neutron Sources*, Nucl. Instrum. Methods Phys. Res., Sect. A **366**, 340 (1995).

[65] T. Tsuruta, T. Niwa, and Y. Fukumoto, *Experimental Study of CR-39 Etched Track Detector for Fast Neutron Dosimetry*, J. Nucl. Sci. Technol. **29**, 1108 (1992).